第 44 卷 第 3 期 焊 接 学 报 Vol. 44(3):98 − 105, 113
2023 年 3 月 TRANSACTIONS OF THE CHINA WELDING INSTITUTION March 2023

电渣堆焊高铬铸铁界面温度场及组织性能

王皓， 胡会娥， 迟钧瀚， 陈泽， 冯子健
(海军工程大学, 武汉, 430022)

摘要: 用电渣堆焊的方法在 D32 低合金钢表面堆焊高铬铸铁硬面层, 测量了堆焊过程中热影响区的温度场, 研究了热影响区、复合界面及硬面层的微观组织和力学性能. 结果表明, 电渣堆焊加热和冷却速度较慢, 稳定阶段时低合金钢基材温度分布均匀, 在堆焊方向最大温度梯度为−21.25 ℃/mm; 低合金钢基板内最大热应力为 53.4 MPa, 低于低合金钢的抗拉强度, 有效避免了裂纹的产生; 复合界面平整清晰, 存在宽度约 50 μm 的奥氏体带状区; 热影响区晶粒有所长大, 为铁素体加珠光体组织; 高铬铸铁硬面层由奥氏体、碳化物和少量马氏体组成, M_7C_3 型碳化物细小且均匀分布于奥氏体晶界; 复合界面结合强度为 96 MPa; 试样熔合区的冲击吸收能量 (53 J) 较硬面层冲击吸收能量 (10.7 J) 明显提高; 亚共晶高铬铸铁硬面层在较大磨损载荷下发生马氏体相变, 硬度提高, 耐磨粒磨损性能优良.

创新点: (1) 综合运用红外热成像和热电偶测温技术监测分析电渣堆焊热过程.
(2) 从组织和性能结果分析论证了电渣堆焊高铬铸铁的可行性.

关键词: 电渣堆焊; 高铬铸铁; 温度场; 微观组织; 耐磨性能
中图分类号: TG 448; TG 402; TG 407 **文献标识码:** A **doi:** 10.12073/j.hjxb.20220418002

0 序言

高铬铸铁具有优异的耐磨损性能, 适用于矿山机械、水泥生产等磨粒磨损场合[1-5]. 但高铬铸铁韧性和止裂性能差, 在承受较大的冲击载荷作用时容易开裂报废. 将高铬铸铁与韧性较好的低合金钢复合, 制成层状金属复合材料, 使工件兼具良好的韧性和表面抗磨损性能, 可大大扩展高铬铸铁的使用范围[6-8].

目前常用的在低合金钢 (或低碳钢) 上复合大尺寸高铬铸铁硬面层的方法有电弧堆焊法[9-10] 和铸造复合法[11-12]. 其中, 电弧堆焊高铬铸铁硬面层时存在极不均匀的温度场和很大的焊接应力, 极易产生裂纹; 而高铬铸铁铸造组织需要进行高温热处理来进一步调控组织、改善性能, 但铸造复合法生产的复合工件为保证整体性能, 不宜进行高温热处理. 因此, 急需一种新的高铬铸铁和低合金钢复合方法, 能够克服以上复合方法的不足, 高效地获得较大尺寸的高质量高铬铸铁硬面层. 电渣焊热输入大, 加热和冷却速度慢, 工件温度分布均匀, 焊接应力较小. Rodionova 等人[13] 用电渣堆焊在低合金钢板表面复合高合金钢硬面层, 界面结合强度高且没有裂纹缺陷. 因此, 可以考虑将电渣堆焊的方法应用于高铬铸铁和低合金钢的复合.

文中用电渣堆焊的方法在低合金钢表面堆焊了高铬铸铁硬面层, 分析探讨了电渣堆焊温度场以及堆焊试样不同部分的组织性能特点, 论证了采用电渣堆焊在低合金钢表面复合高铬铸铁硬面层, 获得无裂纹缺陷、可靠复合界面方法的可行性.

1 试验方法

1.1 堆焊方法

试验用基板为 25 mm 厚的 D32 低合金钢钢板, 熔嘴为外径 10 mm、内径 4 mm 的 ISO101 钢管, 焊剂为 CaF_2-CaO-Al_2O_3 烧结焊剂, 堆焊采用高铬铸铁药芯焊丝. 电渣堆焊如图 1 所示, 熔嘴垂直插入由水冷铜块、低合金钢板和引弧造渣板组成的型腔中, 型腔尺寸 100 mm × 30 mm × 30 mm. 焊接电压 35 ~ 37 V, 焊接电流 300 ~ 320 A. 堆焊过程中, 渣池位于金属熔池上方, 焊丝和熔嘴以及部分

收稿日期: 2022 − 04 − 18
基金项目: 海军工程大学自主立项科研项目 (2022501110)

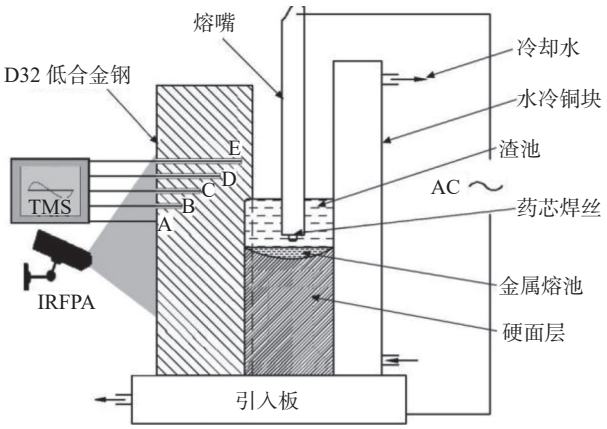

图 1　电渣堆焊装置及测温示意图

Fig. 1　Schematic diagram of electroslag surfacing device and temperature measurement

低合金钢基材在渣池中不断熔化并进入下方的金属熔池，渣池和熔池则不断上升直至电渣堆焊过程结束，最终得到厚度约 30 mm 的电渣堆焊高铬铸铁硬面层．基板、熔嘴钢管和硬面层的化学成分见表 1.

1.2　焊接温度场测量方法

如图 1 所示，用 Sat-HY-G90 型红外热成像仪直观监测堆焊稳定阶段低合金钢背面和上表面的温度场，并绘制等温线图．测量热影响区不同部位的焊接热循环，分别用 ϕ3 mm 钻头在低合金板背面上钻不同深度的盲孔，用储能焊机将 K 型热电偶分别点焊在盲孔端部，热电偶另一端与温度采集装置相连．堆焊时用 LabVIEW 软件进行温度数据的采集，采集频率 100 次/s，采集温度低于 200 ℃ 时结束程序．A 位于低合金钢板表面，B, C, D, E 深度分别为 5, 10, 15 和 20 mm.

表 1　低合金钢基板 D32, ISO101 熔嘴钢管和高铬铸铁硬面层的化学成分 (质量分数，%)

Table 1　Chemical compositions of low alloy steel substrate D32, fusion nozzle steel pipe ISO101 and high chromium cast iron hardfacing layer

材料	C	Si	Mn	Cu	Cr	Ni	V	Mo	Al	Fe
熔嘴	0.08	0.21	0.35	0.08	0.07	0.20	—	—	—	余量
基板	0.13	0.22	1.30	0.32	0.20	0.39	0.08	0.05	0.02	余量
硬面层	2.03	0.68	2.06	0.06	25.33	—	—	0.88	0.07	余量

1.3　微观组织观察和力学性能测试方法

在堆焊试样上取样进行微观组织观察和力学性能测试，取样如图 2 所示．用标准金相制样方法制备金相试样，用光学显微镜和扫描电镜观察硬面层、熔合线以及低合金钢热影响区微观组织，用 Image-Pro-Plus 图像分析软件统计热影响区不同部位晶粒尺寸．用 XRD 检测磨损前后高铬铸铁硬面层的相组成并分别测试其洛氏硬度．按照标准 ISO 148.1—2006 分别测试硬面层、结合界面和热影响区的冲击吸收能量．测量从基材到硬面层的维氏硬度，载荷 490 g，保持时间 15 s．测试高铬铸铁硬面层与低合金钢基体的结合强度，测试时把压头放入试样凹槽中与堆焊层接触，整体安放到 WDW3200 电子万能试验机上进行试验．设定最大载荷为 50 kN，加载速度为 1 mm/min．加载后推力通过压头传递到堆焊层，使堆焊层与基体的结合面承受拉应力，当拉应力超过结合面的结合强度时发生断裂，断裂面应在二者的结合面区域附近，堆焊层与基体的结合强度 σ 为

$$\sigma = F/S \tag{1}$$

式中：F 为断裂瞬间的加载载荷；S 为断裂面面积．

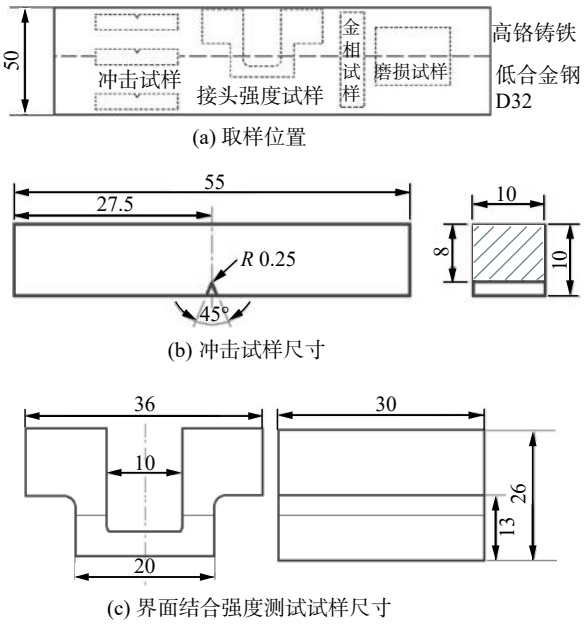

图 2　取样示意图 (mm)

Fig. 2　Schematic diagram of the sampling. (a) sampling position; (b) size of impact specimen; (c) size of interface bonding strength test specimen

依据 ASTM G65—2004 进行磨粒磨损试验, 磨料为石英砂带, 摩擦速度 1.57 m/s, 载荷 100 N, 摩擦时间 200 s. 每组试样分别测 3 次, 用精度为 0.000 1 g 的分析天平分别测量失重并取其平均值.

2 试验结果与分析

2.1 温度场与焊接热循环

在堆焊试样上建立三维坐标轴系, 如图 3 所示. x 方向为堆焊试样宽度方向; y 方向为堆焊硬面层与低合金钢厚度方向, 与复合界面垂直; z 方向为电渣堆焊方向, 堆焊时渣池和金属熔池沿 z 方向向上移动. 图 3a 为堆焊到 z = 50 mm 处稳定阶段时低合金钢基板背面 (x-z 面) 的等温线分布, 图 3b 为堆焊到 z = 100 mm 时低合金钢基板上表面 (x-y 面) 等温线分布.

从图 3a 可以看出, 在 40 mm ≤ z ≤ 60 mm 区间内温度变化平缓, 当 z < 40 mm 和 z > 60 mm 区间内温度下降速度基本恒定; 从图 3b 可以看出温度在 y 轴方向上线性变化. 对试样中的温度梯度进行简化分析, 建立温度分布模型. 假设电渣堆焊稳定状态下某瞬时渣池中心所在高度为 z_0, 渣池厚度为 h, 在试样表面与渣池等高位置温度为 T_0, 渣池热量充分传导到试样表面, 模型可近似认为渣池温度均匀, 则在 $z_0 \pm h/2$ 区间内温度梯度为 0, $z > z_0 + h/2$ 时温度梯度为 θ_{z1}, $z < z_0 - h/2$ 时温度梯度为 θ_{z2}. 在 x 轴方向上, 除去试样边缘小范围的温度陡降区, 温度在整个 x 轴方向上的温度分布比较均

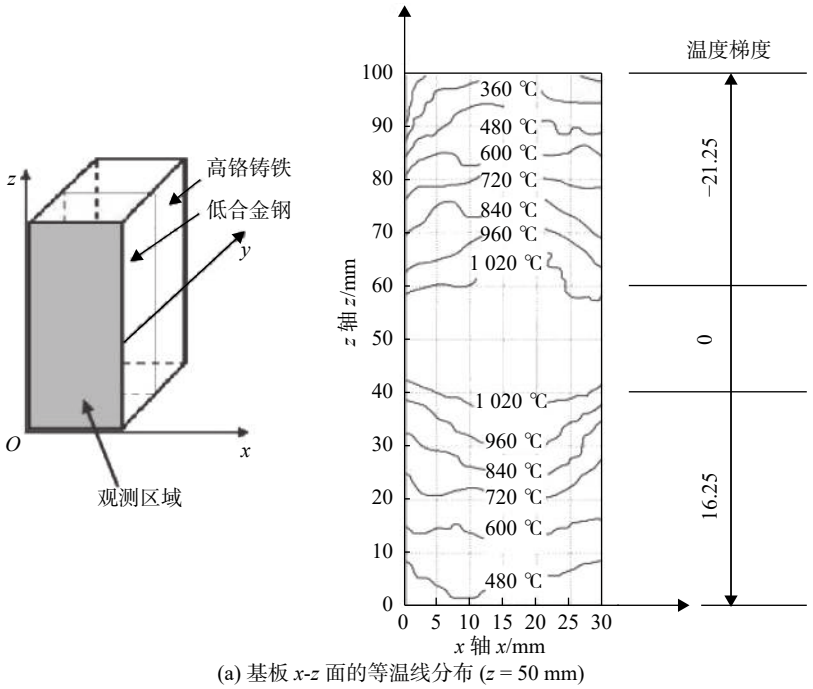

(a) 基板 x-z 面的等温线分布 (z = 50 mm)

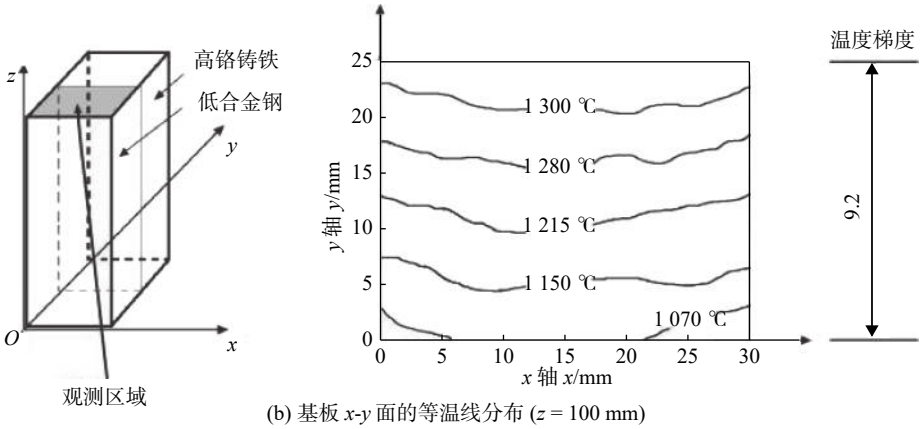

(b) 基板 x-y 面的等温线分布 (z = 100 mm)

图 3 准稳态低合金钢基板表面等温线分布图

Fig. 3 Quasi-steady isotherm distribution diagram of low alloy steel substrate surface. (a) isotherm distribution of substrate x-z plane (z = 50 mm); (b) isotherm distribution of substrate x-y plane (z = 100 mm)

衡，温度梯度 $\theta_x=0$；y 轴方向的温度梯度为 θ_{y0}，可得到此时电渣堆焊低合金钢试样中各点的温度.

$$T_{(x,y,z)}=\begin{cases}T_0+\theta_{y0}y,\ z_0-h/2\leqslant z\leqslant z_0+h/2\\ T_0+\theta_{y0}y+\theta_{z1}(z-z_0-h/2),\ z>z_0+h/2\\ T_0+\theta_{y0}y+\theta_{z2}(z-z_0+h/2),\ z<z_0-h/2\end{cases}\tag{2}$$

根据图 3 可知，当 z_0=50 mm 时，T_0=1 070 ℃；y 轴方向上在 25 mm 厚度范围内，峰值温度从 1 300 ℃降到 1 070 ℃，θ_{y0}=9.2 ℃/mm；z 轴方向上，试样在渣池上方部分的升温主要靠堆焊过程中渣池的热传导，$\theta_{z1}=-21.25$ ℃/mm，试样在渣池下方部分温度的保持靠渣池热传导和堆焊金属凝固时的结晶潜热共同作用，$\theta_{z2}=16.25$ ℃/mm. 将以上初始条件代入式 (2) 可得低合金钢试样的温度分布. 其中，$x\in[0,30]$，$y\in[0,25]$，$z\in[0,100]$.

$$T_{(x,y,z)}=\begin{cases}1\,070+9.2y,\ 40\leqslant z\leqslant 60\\ 1\,070+9.2y-21.25(z-60),\ 60<z\leqslant 100\\ 1\,070+9.2y+16.25(z-40),\ 0\leqslant z<40\end{cases}\tag{3}$$

应力 σ 计算公式为

$$\sigma=E\cdot\varepsilon=E\cdot\alpha\cdot|\theta|\cdot L\tag{4}$$

式中：E 为低合金钢的杨氏模量；α 为线膨胀系数；ε 为应变；θ 为温度梯度；L 取 1 mm. 借助 JMatPro (Java-based Materials Properties software) 软件中的“General Steel”数据库计算 D32 低合金钢在不同温度下的线膨胀系数 α(图 4) 和杨氏模量 E(图 5).

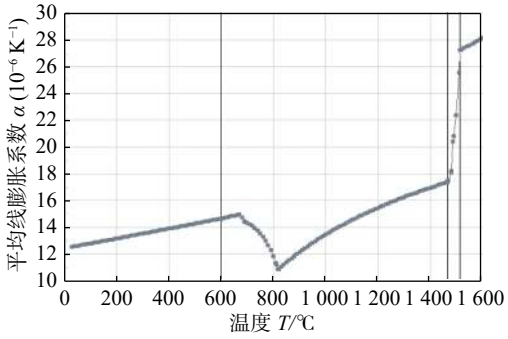

图 4　D32 低合金钢在不同温度下的线胀系数

Fig. 4　Linear expansion coefficient of D32 low alloy steel at different temperatures

将低合金钢内部坐标轴方向温度梯度 θ_x，θ_y，θ_{z1} 和 θ_{z2} 分别代入式 (4)，计算得到低合金钢内部沿各坐标轴的热应力，温度 T 沿 x 轴方向没有变化，即 $T(x,y,z)=T(y,z)$，试样中与 x 轴垂直的 y-z 各相邻平行层面几乎不产生应力. 试样在 y 轴方向热应力为 23.1 MPa，在 z 轴方向温度梯度最大，最大热应力 $\sigma_z=53.4$ MPa. 低合金钢热影响区内不同

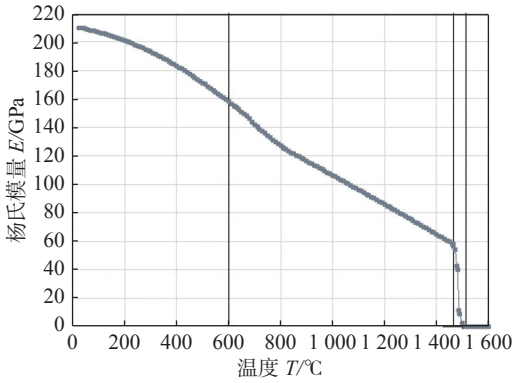

图 5　D32 低合金钢在不同温度下的杨氏模量

Fig. 5　Young's modulus of D32 low alloy steel at different temperatures

方向的热应力均远低于 D32 低合金钢的抗拉强度 440 ~ 570 MPa，不产生裂纹.

电渣堆焊复合高铬铸铁和低合金钢试样如图 6，左侧为高铬铸铁堆焊层，右侧为 D32 低合金钢. 可以看出，堆焊层和基材熔合线在稳定阶段平整清晰，未发现裂纹等缺陷. 从图 6 还可以看出，堆焊试样底部熔合线向硬面层一侧偏离，这是电渣堆焊开始时在底部引弧造渣，大部分热量用于熔化焊剂，产生热量不足以熔化基材所致. 当稳定的渣池建立后，熔合线变得平直.

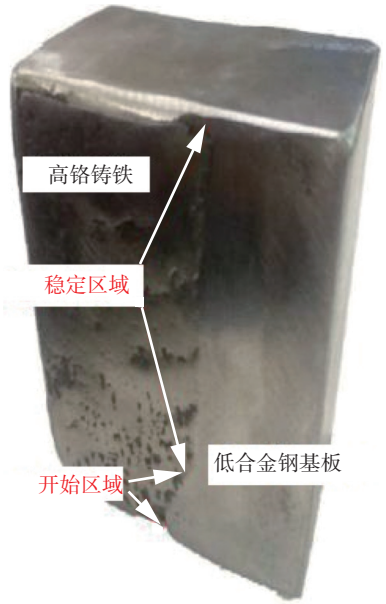

图 6　电渣堆焊试样宏观形貌

Fig. 6　Macromorphology of electroslag surfacing sample

2.2　微观组织

2.2.1　熔合区微观组织

高铬铸铁电渣堆焊层和基材结合界面如图 7. 从图 7a 可以看出，低合金钢和高铬铸铁硬面层的

熔合界面平直. 从图 3a 可以看出, 电渣堆焊时, 作为热源的渣池温度分布较为均匀. 渣池与低合金钢接触面在 x 方向上热流密度分布均匀, 温度梯度 $\theta_x = 0$, 从而使渣池界面处的低合金钢金属同步熔化和凝固, 获得均匀平直的熔合线. 从图 7b 可以看出, 在堆焊层和基材的结合面存在宽度约 50 μm 的奥氏体带状区域. 对图 7b 方框区域进行放大, 可见奥氏体带状区域左侧共晶区分布着短杆状 M_7C_3 型碳化物, 如箭头 a 所示, 这些碳化物不连续分布, 保证了基体的连续性. 奥氏体带状区域右侧与低合金钢熔合线在微观上并不平整, 如箭头 b 所示, 锯齿状界面增加了界面结合面积. 奥氏体相硬度较低, 具有良好的塑韧性, 奥氏体带状区域的存在有助于提高结合界面的断裂韧性和结合强度.

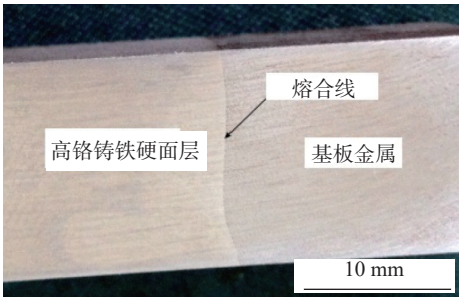

(a) 宏观形貌

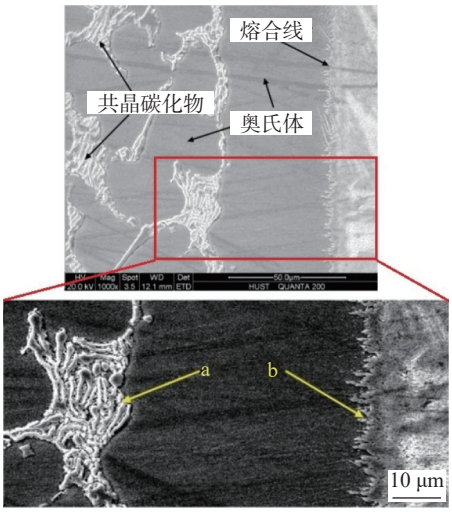

(b) 界面处微观组织

图 7 高铬铸铁电渣堆焊层和基材结合界面

Fig. 7 Interface of surfacing layer and substrate. (a) macromorphology; (b) microstructure at the interface

2.2.2 低合金钢基材热影响区微观组织

对于普通的低合金钢, 其晶粒急剧长大的开始温度约为 1 100 ℃, 从图 8 和表 2 可以看出, 低合金钢中测试点 B, C, D, E 的峰值温度均超过 1 100 ℃, 因此 B, C, D, E 均处于粗晶区, 其显微组织均含有魏氏组织. 图 9 为低合金钢热影响区不同区域的金相组织, 根据 GB/T 13299—1991《钢的显微组织评定方法》对不同位置的组织进行分级, 图 9a 为低合金钢测温点 E 处的金相组织, 该区域紧邻熔合线, 堆焊时峰值温度达到 1 300 ℃, 1 000 ℃ 以上高温停留时间约 182 s, 奥氏体晶粒长得非常粗大, 冷却后形成粗大针状及厚网状的非常明显的魏氏体组织, 为 A4 级魏氏组织; 图 9b 中低合金钢测温点 D 处为 A3 级魏氏组织, 可见铁素体网向晶内生长, 呈针状分布于晶粒内部; 图 9c 低合金钢测温点 C 处为 A2 级魏氏组织, 块状铁素体间隙出现个别针状组织区; 图 9d 低合金钢测温点 B 处为 A1 级组织, 铁素体组织中呈现不规则的块状铁素体; 图 9e 低合金钢测温点 A 处为 A1 级组织, 为均匀的铁素体和珠光体组织. 测试点 A 的峰值温度为 1 070 ℃, 处于 A_{c3} 到晶粒急剧长大温度 1 100 ℃ 之间, 该区域在加热和冷却过程中经受了两次重结晶相变的作用, 晶粒显著细化, 其平均晶粒尺寸只有 3 μm, 显微组织没有魏氏组织特征.

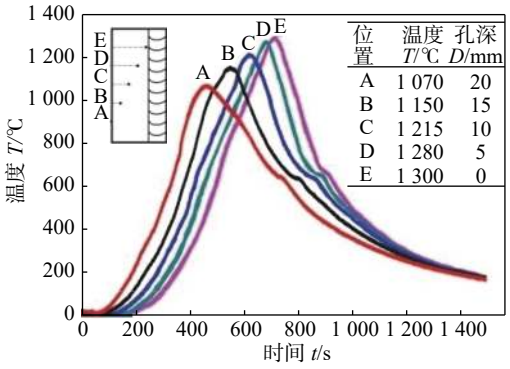

图 8 低合金钢 y 轴方向不同部位热循环曲线

Fig. 8 Thermal cycle curve of different parts in y-axis direction of low alloy steel

表 2 电渣堆焊过程焊接热循环特征参数

Table 2 Characteristic parameters of welding thermal cycle during electroslag surfacing

位置	峰值温度 T_{max}/℃	高温停留时间 (T = 1 000 ℃) t/s	800 ~ 500 ℃ 冷却时间 $t_{8/5}$/s	平均晶粒直径 d/μm
A	1 070	56	209	3
B	1 150	143	208	47
C	1 215	156	205	105
D	1 280	169	201	173
E	1 300	182	199	228

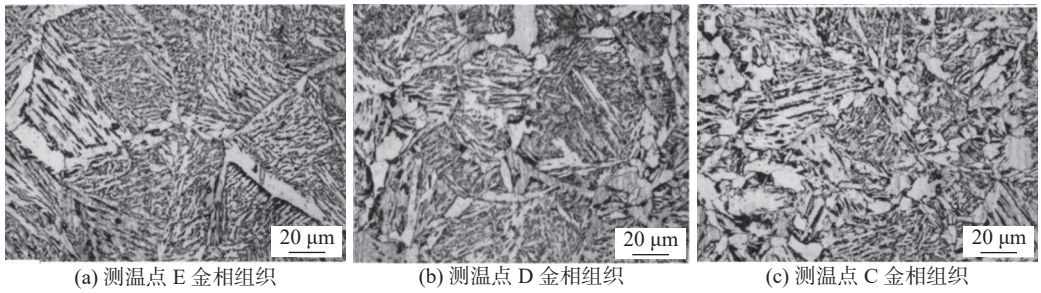

(a) 测温点 E 金相组织　(b) 测温点 D 金相组织　(c) 测温点 C 金相组织

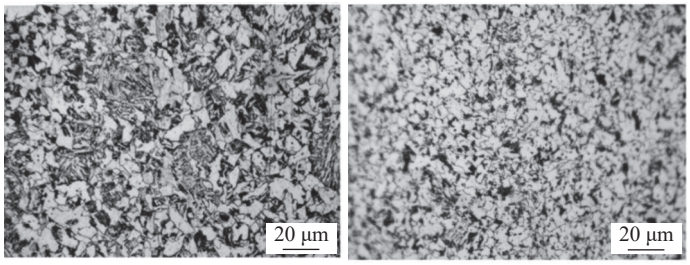

(d) 测温点 B 金相组织　(e) 测温点 A 金相组织

图 9　低合金钢 D32 热影响区微观组织

Fig. 9　Microstructures of heat affected zone of low alloy steel D32. (a) at measuring point E; (b) at measuring point D; (c) at measuring point C; (d) at measuring point B; (e) at measuring point A

2. 2. 3　硬面层微观组织

图 10 为高铬铸铁硬面层表面向下 3 mm 处金相组织照片，为硬面层显微组织. 从图 10a 可以看出高铬铸铁硬面层中含有大量的团块状初晶奥氏体，从图 10b 可以看出在初晶奥氏体晶界分布着共晶组织，共晶组织中 M_7C_3 型碳化物呈杆状或长条状均匀分布在初晶奥氏体晶界处，硬面层组织均匀. 如图 11 所示，XRD 分析结果表明复合硬面层由奥氏体相、M_7C_3 型碳化物相和马氏体相组成.

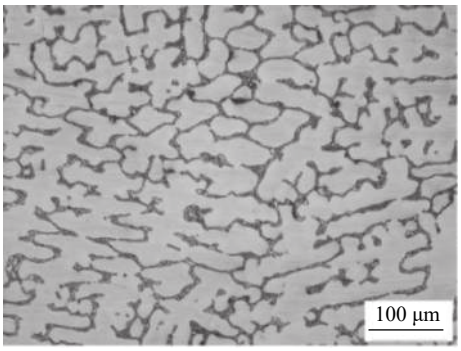

(a) 硬面层金相组织 (低倍)

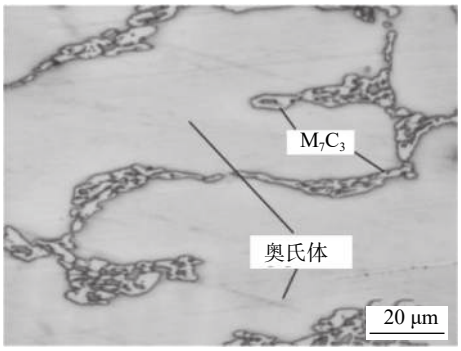

(b) 硬面层金相组织 (高倍)

图 10　高铬铸铁硬面层金相组织

Fig. 10　Microstructure of high chromium cast iron hardfacing layer. (a) microstructure (low); (b) microstructure (high)

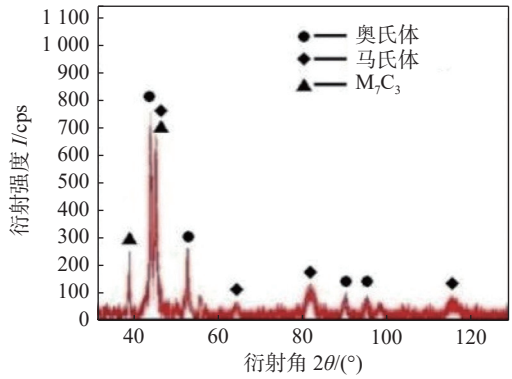

图 11　高铬铸铁硬面层 XRD 分析

Fig. 11　XRD analysis of high chromium cast iron hardfacing layer

2.3　力学性能

2. 3. 1　硬度

图 12 为低合金钢基材、热影响区、熔合区和高铬铸铁硬面层的显微硬度图. 热影响区的 $t_{8/5}$ 时间大于 180 s，在冷却过程中整个试样冷却缓慢，没有马氏体的产生，硬度在 330 ~ 400 HV 之间，其中过热区存在粗大的魏氏组织，硬度较高，达到了 400 HV，离熔合线距离增加，晶粒细化，魏氏组织减

少，硬度随之降低；在热影响区细晶区晶粒比较细小，综合力学性能好，硬度略有提高；在熔合区，高铬铸铁中的碳元素向低合金钢中扩散，硬度随碳含量的增多明显升高；堆焊硬面层发生亚共晶转变，共晶碳化物程颗粒状分布在奥氏体基体上，硬度达到了 700 HV，约为低合金钢 D32 硬度的 2 倍.

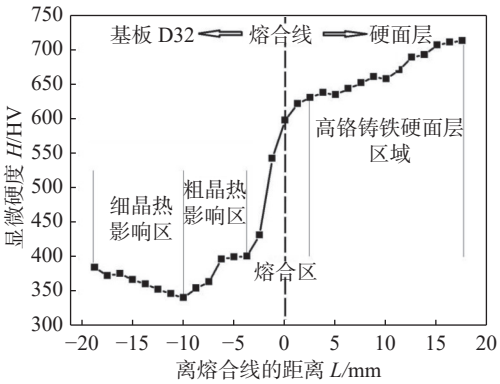

图 12 试样显微硬度变化曲线

Fig. 12 Microhardness change curve of sample

2.3.2 界面结合强度

测定熔合界面的结合强度，当载荷 F 为 14.4 kN，试样发生断裂，断裂面面积 S 为 150 mm^2，计算得到断裂强度 σ 为 96 MPa. 图 13 是试样断裂位置及其断口特征. 图 13a 为断口侧边宏观形貌，裂纹首先在高铬铸铁堆焊层中萌生，裂纹萌生位置距离堆焊层与基材界面约 1 mm，而后裂纹在高铬铸铁堆焊层中扩展，到达熔合界面后沿界面扩展，直至到达试样表面. 在裂纹扩展到熔合界面处产生次生裂纹，次生裂纹进入低合金钢粗晶热影响区，扩展到细晶热影响区停止，并没有贯穿到试样表面. 可见，低合金钢与高铬铸铁结合界面并不是熔合区最薄弱环节，结合强度满足使用要求. 图 13b 为断口的微观形貌特征，高铬铸铁为脆硬性材料，裂纹断面存在较多穿晶断裂解离面，解离面之间形成河流状花样，为解离性脆性断裂. 但由于高铬铸铁硬面层中含有较多的初晶奥氏体，韧性相对较高，如图 13b 中箭头所示，在界面层存在少量塑性变形后留下的撕裂状形貌.

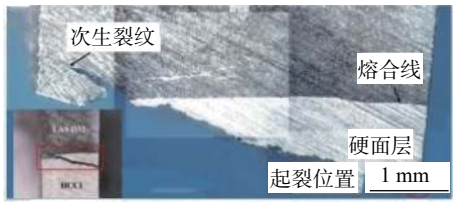

(a) 断口侧边宏观形貌

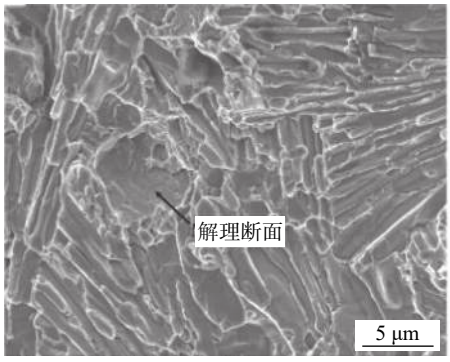

(b) 断口微观形貌

图 13 推离试样断口形貌

Fig. 13 Fracture morphology of push-off sample. (a) macromorphology of the fracture; (b) microstructure of the fracture

2.3.3 冲击韧性

分别在高铬铸铁硬面层、低合金钢基材，复合界面熔合区和细晶热影响区取冲击试样，测得各部分的室温 (25 ℃) 冲击吸收能量见表 3. 热影响区不同区域的冲击韧性差别较大，细晶区的晶粒细小均匀，其冲击韧性甚至好于基材，该区域的冲击吸收能量为基材的 116%，而复合界面熔合区包含粗晶热影响区，粗大的魏氏组织使得熔合区冲击吸收能量只有低合金钢基材的 32%，但仍为高铬铸铁硬面层的冲击韧性的 5 倍，复合后冲击韧性明显提高.

表 3 复合试样不同位置的冲击吸收能量 A_{kv}(25 ℃)(J)

Table 3 Impact absorption energy at different positions of the composite specimen A_{kv}(25 ℃)

测试区	试样1	试样2	试样3	平均值
D32	166	162	164	164.0
熔合区	46	58	55	53.0
细晶热影响区	190	193	186	189.7
硬面层	11	10	11	10.7

2.3.4 耐磨性能

磨粒磨损试验测得高铬铸铁电渣硬面堆焊层摩擦平均失重为 0.256 1 g，图 14 为磨损表面形貌. 可见磨损面犁沟细小且分布均匀，没有发现开裂和硬面层剥离现象，说明硬面层具有一定塑韧性和较高的硬度，在较大摩擦载荷下具有优良的耐磨粒磨损性能. 对比图 11 和图 15 的 XRD 分析结果，可以发现磨损后硬面层中奥氏体相含量降低，马氏体相含量增多，磨损前硬面层洛氏硬度为 46 HRC±3 HRC，磨损后硬面层洛氏硬度为 53 HRC±5 HRC，磨损后硬面层平均硬度提高了 7 HRC. 这是因为奥氏体韧性较好，磨损过程中奥氏体在承受较大冲击载荷时发生了马氏体相变，使得硬面层硬度和耐磨

损性能提高. 因此, 在承受较大冲击载荷的磨粒磨损条件下, 具有奥氏体基体的电渣堆焊高铬铸铁硬面层有良好的耐磨损性能.

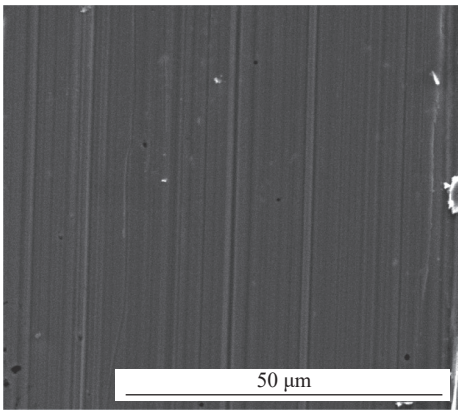

图 14　硬面层磨损形貌

Fig. 14　Wear morphology of hardfacing layer

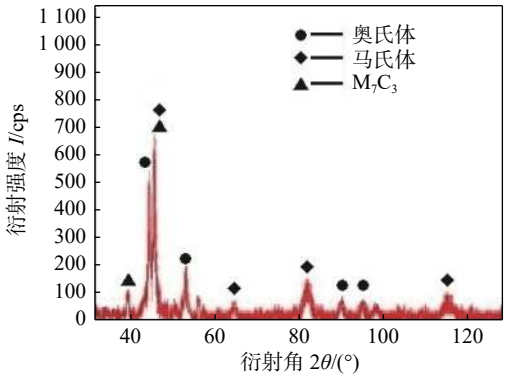

图 15　磨损试样磨损面 XRD 分析

Fig. 15　XRD analysis of wear surface

3　结论

(1) 电渣焊热输入大, 用电渣堆焊的方法在低合金钢 D32 表面复合高铬铸铁硬面层, 工件温度分布均匀, 温度梯度小, 可避免硬面层和结合界面产生裂纹.

(2) 电渣堆焊时热影响区焊接热循环峰值温度 1 100 ℃ 以上区域为粗晶区, 其 $t_{8/5}$ 时间大于 180 s, 没有马氏体, 但含有魏氏组织; 在高铬铸铁硬面层和低合金钢界面形成宽度约 50 μm 的奥氏体带状区, 可有效提高界面韧性和结合强度; 高铬铸铁硬面层组织稳定, 含有大量的奥氏体组织.

(3) 电渣堆焊高铬铸铁/低合金钢复合试样冲击韧性较高铬铸铁硬面层冲击韧性提高了 5 倍; 界面结合力测试时, 断裂发生在高铬铸铁硬面层一侧, 断裂强度 96 MPa; 电渣堆焊高铬铸铁硬面层中奥氏体在 100 N 摩擦载荷下发生马氏体相变, 磨损前后硬面层硬度提高了 7 HRC, 具有良好的耐磨损性能.

参考文献

[1] Tang X H, Chung R, Pang C J, *et al*. Microstructure of high (45wt.%) chromium cast irons and their resistances to wear and corrosion[J]. Wear, 2011, 271(9): 1426 − 1431.

[2] Tang X H, Chung R, Li D Y, *et al*. Variations in microstructure of high chromium cast irons and resultant changes in resistance to wear, corrosion and corrosive wear[J]. Wear, 2009, 267(1): 116 − 121.

[3] 苏允海, 梁学伟, 邓越, 等. FeAlCuCrNiNbx 系高熵合金堆焊层的组织及性能分析 [J]. 焊接学报, 2020, 41(4): 38 − 43,50.
Su Yunhai, Liang Xuewei, Deng Yue, *et al*. Microstructure and property analysis of FeAlCuCrNiNbx high-entropy alloy surfacing layer[J]. Transactions of the China Welding Institution, 2020, 41(4): 38 − 43,50.

[4] Wang S, Li Y M, Wang J, *et al*. Effect of in-situ (Ti & W) C multiphase particles on three-body abrasive wear of high chromium cast iron[J]. Materials Chemistry and Physics, 2023, 295(2): 127 − 161.

[5] Feng A X, Wei Y C, Liu B J, *et al*. Microstructure and mechanical properties of composite strengthened high-chromium cast iron by laser quenching and laser shock peening[J]. Journal of Materials Research and Technology, 2022, 20: 4342 − 4355.

[6] 魏建军, 黄智泉, 杨威. 高碳高铬铸铁堆焊合金组织分析 [J]. 焊接学报, 2008, 29(3): 145 − 148.
Wei Jianjun, Huang Zhiquan, Yang Wei. Microstructures of high chromium cast iron for surfacing[J]. Transactions of the China Welding Institution, 2008, 29(3): 145 − 148.

[7] Chatterjee S, Pal T K. Weld procedural effect on the performance of iron based hardfacing deposits on cast iron substrate[J]. Journal of Materials Processing Technology, 2006, 173(1): 61 − 69.

[8] Sapate S G, RamaRao A V. Erosive wear behaviour of weld hardfacing high chromium cast irons: effect of erodent particles[J]. Tribology International, 2006, 39(3): 206 − 212.

[9] Liu J B, Wang L M, Liu J H. Influence of process parameters on microstructure of reactive plasma cladding TiC-Fe-Cr coating[J]. China Welding, 2021, 30(2): 35 − 41.

[10] 刘西洋, 孙凤莲, 王君宇, 等. 自保护药芯焊丝激光-电弧复合热源堆焊参数对焊道表面成形的影响 [J]. 焊接学报, 2018, 39(3): 83 − 88.
Liu Xiyang, Sun Fenglian, Wang Junyu, *et al*. Influence of the surfacing process of laser-arc hybrid welding with self-shielded flux-cored wire on the bead appearance[J]. Transactions of the China Welding Institution, 2018, 39(3): 83 − 88.

[下转第 113 页]

of welding technologies for thick metal plate welds[J]. Journal of Cleaner Production, 2015, 108: 46 − 53.

[2] Liu Wenji, Li Liangyu, Yue Jianfeng, *et al*. Research on the "jump sidewall" behavior and its signal characteristics in narrow gap P-MAG welding[J]. The International Journal of Advanced Manufacturing Technology, 2017, 91(1-4): 1189 − 1196.

[3] 洪波, 戴威, 李湘文, 等. 窄间隙埋弧焊的磁控与电感复合式焊缝跟踪方法 [J]. 焊接学报, 2016, 37(1): 11 − 14.
Hong Bo, Dai Wei, Li Xiangwen, *et al*. Magnetic control and inductance combined welding seam tracking method for narrow gap submerged arc welding[J]. Transactions of the China Welding Institution, 2016, 37(1): 11 − 14.

[4] Yang Wuxiong, Xin Jijun, Fang Chao, *et al*. Microstructure and mechanical properties of ultra-narrow gap laser weld joint of 100 mm-thick SUS304 steel plates[J]. Journal of Materials Processing Technology, 2019(25): 130 − 137.

[5] Liu Guoqiang, Tang Xinhua, Han Siyuan, *et al*. Influence of inter-wire distance and arc length on welding process and defect formation mechanism in double-wire pulsed narrow-gap gas metal arc welding[J]. Journal of Materials Engineering and Performance, 2021(30): 7622 − 7635.

[6] 洪波, 言浚光, 阳佳旺, 等. 一种用于焊缝跟踪的电容式传感器 [J]. 焊接学报, 2014, 35(2): 55 − 58.
Hong Bo, Yan Junguang, Yang Jiawang, *et al*. A capacitive sensor for welding seam tracking[J]. Transactions of the China Welding Institution, 2014, 35(2): 55 − 58.

[7] 李湘文, 陶韬, 洪波, 等. 基于薄板搭接的摆动式相邻电容焊缝跟踪传感器 [J]. 焊接学报, 2017, 38(9): 61 − 64.
Li Xiangwen, Tao Tao, Hong Bo, *et al*. Swing type adjacent capacitor welding seam tracking sensor based on thin plate lap joint[J]. Transactions of the China Welding Institution, 2017, 38(9): 61 − 64.

[8] 洪波, 朱亚飞, 李湘文, 等. 电容电感复合桥式焊缝跟踪传感器 [J]. 焊接学报, 2015, 36(4): 9 − 12.
Hong Bo, Zhu Yafei, Li Xiangwen, *et al*. Capacitance and inductance composite bridge welding seam tracking sensor[J]. Acta China Welding Institution, 2015, 36(4): 9 − 12.

[9] 王大伦. 电动力学教程 [M]. 湘潭: 湘潭大学出版社, 2017: 47-48.
Wang Dalun. Electrodynamics tutorial[M]. Xiangtan: Xiangtan University Press, 2017: 47-48.

[10] 谢东, 李昌禧. 同面散射场电容式砂含水量传感器的研究 [J]. 传感技术学报, 2008, 21(12): 2000 − 2004.
Xie Dong, Li Changxi. Research on capacitive sand moisture content sensor with co-planar scattering field[J]. Journal of Sensor Technology, 2008, 21(12): 2000 − 2004.

[11] 吴云靖, 董恩生, 庞宇, 等. 基于 ANSYS 的同面多电极电容传感器仿真研究 [J]. 计测技术, 2010, 30(4): 9 − 11.
Wu Yunjing, Dong Ensheng, Pang Yu, *et al*. Simulation research of multi-electrode capacitance sensor on the same plane based on ANSYS[J]. Measurement Technology, 2010, 30(4): 9 − 11.

[12] 黄林, 陈向东, 谢宁宁, 等. 基于 AD7150 微位移电容传感器的研究 [J]. 半导体技术, 2012, 37(6): 425 − 428.
Huang Lin, Chen Xiangdong, Xie Ningning, *et al*. Research on micro displacement capacitance sensor based on AD7150[J]. Semiconductor technology, 2012, 37(6): 425 − 428.

[13] Schmitt D, Novak J, Maslakowski J, *et al*. Automating a precision braze paste dispensing operation using non-contact sensing[R]. Albuquerque: Sandia National Labs, 1993.

第一作者: 李湘文，博士，副教授；主要从事焊接机器人和自动化、焊接工艺及设备等方面的科研和教学工作；发表论文 20 余篇；Email: xwlee@xtu.edu.cn.

（编辑：　曲畅）

[上接第 105 页]

[11] Xie G, Sheng H, Han J T, *et al*. Fabrication of high chromium cast iron/low carbon steel composite material by cast and hot rolling process[J]. Materials & Design, 2010, 31(6): 3062 − 3066.

[12] Xiong B W, Cai C C, Wang H, *et al*. Fabrication of high chromium cast iron and medium carbon steel bimetal by liquid-solid casting in electromagnetic induction field[J]. Materials & Design, 2011, 32(5): 2978 − 2982.

[13] Rodionova I G, Sharapov A A, Puzachev V I, *et al*. Use of electroslag hard-facing to improve the quality of corrosion-resistant bimetal[J]. Chemical and Petroleum Engineering, 1998, 34(2): 139 − 143.

第一作者: 王皓，博士；主要研究方向为舰船高能焊接；Email: qiaowanghao@126.com.

（编辑：　高忠梅）

spectively. The microstructure of the surfacing alloy with 5% Ti is the smallest. Tic or NbC hard phase particles are evenly dispersed in the structure and can be used as wear-resistant particles to form a wear-resistant skeleton with refined primary austenite and eutectic structure to jointly resist the wedging and cutting effect of wear particles. When the content of Ti is 5%, the surfacing alloy containing Ti achieves the best wear resistance, the hardness is 66 HRC and the wear amount is 0.048 7 g; When the addition of Nb is 4%, the surfacing alloy containing Nb achieves the best wear resistance, the hardness is 65 HRC and the wear amount is 0.052 4 g. Under the same conditions, the iron-based surfacing alloy containing an appropriate amount of Ti has better wear resistance.

Highlights: (1) The Fe-Cr-C-B iron-based surfacing alloy containing Ti or Nb is prepared by open arc surfacing with self-shielded flux-cored wire.
(2) The effect of Ti or Nb on the micro-structure and properties of Fe-Cr-C-B iron-based surfacing alloy was analyzed.
(3) Comparing the strengthening effect of TiC and NbC hard phase particles, the Fe-Cr-C-B iron-based surfacing alloy has the best wear-resistance.

Key words: iron base surfacing alloy; self-protective flux cored wire; open arc surfacing; microstructure and properties; TiC and NbC particles

Development of high power low ripple plasma spray chopper power supply WANG Dianlong[1], HUANG Hao[1], ZOU Xianxin[1], LIANG Zhimin[1], WU Chaojun[2](1. Hebei Provincial Key Laboratory of Material Near-net Forming Technology, Hebei University of Science and Technology, Shijiazhuang 050000, China; 2. Institute of Aerospace Materials and Technology, Beijing 100076, China). pp 92-97

Abstract: Plasma spraying power supply usually adopts thyristor rectifier power supply or inverter power supply, which has problems such as low efficiency and large output current ripple. It is difficult to meet the special requirements of plasma spraying process. A high-power plasma spray chopper power supply was proposed based on an eight-phase interleaved parallel Buck converter in this paper. Firstly, the circuit topology of the chopper power supply was designed. The working principle and the current ripple generation mechanism of the chopper power supply were analyzed. The influence of the number of parallel phases and the duty cycle on the current ripple was clarified. The simulation verification was carried out. Then, based on the requirements of the plasma spraying process for power supply characteristics, a four-phase interleaved parallel module with power of 40 kW was designed. Under the cooperative control of the CAN bus, an 80 kW eight-phase interleaved parallel chopper plasma spraying power supply was formed. Finally, the plasma spraying chopper power supply prototype was built. Spraying experiments were carried out to test the output ripple and efficiency of the power supply. The experimental results show that, compared with the traditional thyristor rectifier power supply and inverter power supply, the current ripple rate of the chopper power supply was reduced by more than 50%, and the power efficiency was up to 94.5%.

Highlights: (1) A plasma spray chopper power supply based on an eight-phase interleaved parallel Buck converter was proposed.
(2) Based on plasma spray chopper power supply, the controller of eight-phase interleaved parallel Buck converter was designed.

Key words: plasma spray; chopper power supply; Buck converter; interleaved parallel; current ripple

Study on temperature field, microstructure and properties of electroslag surfacing high chromium cast iron WANG Hao, HU Huie, CHI Junhan, CHEN Ze, FENG Zijian(Naval Engineering University, WuHan 430022, China). pp 98-105,113

Abstract: In this paper, the high chromium cast iron (HCCI) hardfacing layer is deposited on the surface of D32 low-alloy steel by electroslag surfacing method. Combined with the temperature field measurement of the heat-affected zone (HAZ) during the surfacing process, the microstructure and mechanical properties of the HAZ, composite interface and hardfacing layer are studied. The results show that: the heating and cooling rates are slower during the electroslag surfacing, and the temperature distribution in the low alloy steel substrate during the stabilizing stage is uniform; the maximum temperature gradient in the surfacing direction is 23.1 ℃/mm. The maximum thermal stress in the low-alloy steel substrate is 25.9 MPa, lower than its tensile strength, which effectively avoids the occurrence of cracks; the composite interface is smooth and clear, with an austenite band region, about 50 μm in width; The grains of HAZ have grown, whose microstructure is a mixture of ferrite and pearlite. The microstructure of HCCI hardfacing layer is composed of austenite, carbides and a small amount of

martensite. The M_7C_3 type carbides are small and uniformly distributed in austenite grain boundaries. The bonding strength of the composite interface is 96 MPa; the impact energy (53 J) of the composite sample is significantly higher than that of the HCCI hardfacing layer (10.7 J). During abrasion, the HCCI hardfacing layer undergoes martensitic transformation under a large load, the hardness is improved, and an excellent performance in wear resistance was obtained.

Highlights: (1) Comprehensive use of infrared thermography technology and thermocouple temperature measurement technology to monitor and analyze the thermal process of electroslag surfacing.
(2) The feasibility of electroslag surfacing of high chromium cast iron was demonstrated from the analysis of microstructure and performance results.

Key words: electroslag surfacing; high chromium cast iron; temperature field; microstructure; properties

A cylindrical capacitance sensor suitable for automatic arc tracking system of narrow gap weld LI Xiangwen[1], WANG Lu[1], YI Chushan[2], WU Jiayun[2], LONG Zhiheng[3](1. Welding robot and its application Key Laboratory of Hunan Province, Xiangtan University, Xiangtan 411105, China; 2. China Aviation Development South Industries Co., Ltd., Zhuzhou 412000, China; 3. Xiangtan University, Xiangtan 411105, China). pp 106-113

Abstract: Seam tracking system is one of the key technology to realize intelligent welding. Aiming at the problems of welding seam tracking in narrow gap, such as the difficulty of real time seam tracking weld seam of sensor, a new multipole array capacitive sensor based on fringe electric field technology is designed. And the welding seam surface reconstruction is realized through the capacitive signal processing technology based on wavelet filtering and nonlinear mapping technology. Firstly, a mathematical model of multipole array capacitive sensing is established, and the capacitive sensor structure is optimized through theory calculation results and finite element simulation analysis. Subsequently,The capacitive signal of the sensor is extracted and optimized with the help of capacitance signal processing technology, the welding gun offset,and weld deviation are both obtained. The results show that the reconstructed weld surface is basically the same as the narrow gap weld in the experiment, and it is feasible for the multipole array capacitive sensor applying to narrow gap weld tracking, which is of great significance for narrow gap weld tracking.

Highlights: (1) A multi-pole array capacitive sensor based on edge electric field technology is designed.
(2) The sensor is used to reconstruct the bevel shape of narrow gap welds.

Key words: narrow gap welding; cylindrical capacitance sensor; seam tracking; capacitance signal processing

Effect of scanning characteristic parameters on surface morphology of selective laser melting 316L ZHU Chunxia, QIU Bojie(Shenyang Jianzhu University, Shenyang 110168, China). pp 114-121,128

Abstract: In order to study the influence of different scanning characteristic parameters on the surface morphology of selective laser melting (SLM), 316L stainless steel powder was taken as an example to carry out the single-layer and double-track numerical simulation at the mesoscopic scale. Based on the Discrete Element Method, the numerical model of powder bed is established. The Volume of Fluid method is used to calculate the melting, flow and solidification process of heated powder in powder bed. Considering the three scanning characteristic parameters of laser power, scanning speed and scanning spacing, the orthogonal experiment was designed and carried out to study the influence of selected scanning characteristic parameters on the tracks morphology on the surface of the formed part was studied from the two aspects of the tracks morphology and the tracks width. The effectiveness of numerical simulation was verified by actual printing and morphology observation experiments. The results show that in the range of linear energy density of 313 ~ 500 J/m and scanning interval of 50 ~ 90 μm, the morphology of melting tracks with smooth continuous local defects can be obtained, and the parameter combination in this interval is linearly corresponding in turn. In terms of the influence on the integrity of the weld morphology, scanning speed > scanning spacing > laser power.

Highlights: (1) Research on the influence of process parameters on the morphology of melt channels from the perspective of multi-melt channel forming under mesoscopic.
(2) Verification of numerical results by using the method of non-sectional image observation of melt channel and numerical results for mutual comparison.

Key words: selective laser melting; tracks morphology; single-layer double-channel; numerical simulation